RSC Advances

PAPER

View Article Online
View Journal | View Issue

Cite this: *RSC Adv.*, 2024, **14**, 26050

Detection of low-concentration heavy metal exploiting Tamm resonance in a porous TiO_2 photonic crystal

Asmaa M. Elsayed,[a] Ashour M. Ahmed,[bd] Arafa H. Aly, *[ac] M. F. Eissa[d] and M. T. Tammam[d]

The detection of heavy metal ions, particularly Hg^{2+}, has gained significant attention due to their severe adverse effects on human health and ecosystems. Conventional methods for monitoring these metals in freshwater often suffer from limitations in sensitivity, accuracy, and cost-effectiveness. This work introduces a novel heavy metal sensor based on Tamm resonance within a one-dimensional (1D) porous TiO_2 photonic crystal structure. The sensor design includes a prism, a silver (Ag) layer, a cavity, and a ternary multilayer porous TiO_2 layer. Reflectance spectra are analyzed using the transfer matrix method. A key aspect of this study is the optimization of sensor performance, which involves adjusting the thicknesses of all layers and the porosity of the multilayer porous TiO_2. This optimization strategy is critical for achieving high sensitivity. The results demonstrate that the optimized sensor exhibits a high sensitivity of 0.045 nm ppm^{-1} for Hg^{2+} solutions. This sensitivity arises from the effective integration of Tamm resonance with the properties of the porous TiO_2 photonic crystal. The proposed structure shows great potential for applications in heavy metal sensing, especially for detecting Hg^{2+} ion contamination in drinking water with high sensitivity and accuracy. In addition to its high performance, the photonic crystal sensor offers extended lifetime, rapid measurement capabilities, cost-effectiveness, and potential for integration into compact devices, making it a promising solution for environmental monitoring and water quality assessment.

Received 15th July 2024
Accepted 13th August 2024

DOI: 10.1039/d4ra05116e

rsc.li/rsc-advances

1. Introduction

Over the past few decades, water quality has significantly deteriorated worldwide due to population growth, quick growth in industrialization, expanding urbanization, and also unsustainable utilization of natural resources.[1,2] Shockingly, an estimated 14 000 individuals lose their lives each day due to causes related to water pollution.[3] The contamination of water with heavy metals has significantly increased owing to rapid industrial, agricultural, and domestic practices.[4,5]

Heavy metals include chromium, lead, cadmium, mercury, arsenic, nickel, and copper are dense metallic elements that pose a threat.[6] Such heavy metals are not biodegradable and therefore tend to accumulate in living organisms through a process called bioaccumulation.[7,8] Even at low concentrations, heavy metal ions can be carcinogenic to humans and can damage multiple organs. Exposure to mercury (Hg^{2+}) ions can lead to a range of health effects and diseases.[9,10] These include central nervous system defects, erethism, cardiomyopathy, lymphoproliferation, hyporeactivities, neurological issues, nephrological problems, immunological dysfunctions, motor impairments, and genetic disorders. Additionally, it can impact organs such as the brain, lungs, and immune system. Furthermore, mercury exposure has been linked to birth defects, impotency, and infertility.[11] Therefore, the development of efficient technologies to detect heavy metals in water is crucial. Various spectroscopic techniques including X-ray fluorescence (XRF), atomic absorption (AAS), inductively coupled plasma mass spectrometry (ICP-MS), and inductively coupled plasma optical emission (ICP-OES) spectroscopies have been employed for this purpose.[12–14] However, these spectroscopic techniques have limitations in terms of sensitivity, accuracy, cost, and ecological impact.[15,16] On the other hand, electrochemical techniques provide alternative detection methods, including potentiometric, amperometric, voltammetric, coulometric, impedance, and electrochemiluminescent measurements. It is necessary to notice that electrochemical techniques may not be the most suitable choice when multiple metal cations are simultaneously present in a sample, as this can lead to reduced detection sensitivity.[17]

[a]TH-PPM Group, Physics Department, Faculty of Science, Beni-Suef University, Beni-Suef 62514, Egypt. E-mail: arafaaly@aucegypt.edu; arafa.hussien@science.bsu.edu.eg

[b]Physics Department, College of Science, Imam Mohammad Ibn Saud Islamic University (IMSIU), Riyadh 11623, Saudi Arabia

[c]Department of Technical Sciences, Western Caspian University, Baku 1001, Azerbaijan

[d]Faculty of Science, Beni-Suef University, Beni-Suef 62514, Egypt

Optical technologies offer several benefits, including extended sensor lifetimes, rapid measurement capabilities, and cost-effectiveness.[4,18] Among these technologies, photonic crystals (PCs) stand out as a revolutionary optical technology.[19] PCs are composed of periodic structures that vary the refractive index of a material on the scale of the wavelength of light.[20,21] This allows PCs to regulate the light behavior, similar to how semiconductors manipulate electrons. Photons passing through a photonic crystal experience frequency band gaps, which give rise to unique optical properties known as photonic bandgaps (PBGs).[22–24] The presence of PBGs in photonic crystals enables precise control over the propagation. This control offers a range of advantages for sensor applications, including improved sensitivity, versatility, and integration into small, compact devices. These unique properties make PCs highly promising candidates for a wide range of sensor applications.[25,26]

Recently, sensor systems have increasingly utilized PCs for various applications.[27] Lu *et al.*[28] proposed the use of inverse opal polymeric photonic crystals (IOPPCs) with effective urease catalysis and pH-responsive characteristics. Their research achieved a minimum detectable concentration of 5×10^{-16} g L^{-1}.[28] Taha *et al.* also proposed a model of a PC consisting of gyroidal Ag and TiO_2 for detecting Cu^{2+} and Mg^{2+} ions. This PC design achieved sensitivity values of 573.50 and 570.70 nm RIU^{-1}, respectively.[29] Additionally, Chou *et al.* presented a method for detecting heavy metal ions using PCs composed of polymer brushes, in conjunction with a reflective laser beam system, achieved a low detection limit of 10 μg L^{-1} for Cr(III).[30] These studies demonstrate the promising potential of PCs in detecting low concentrations of contaminants in water.[31]

The one-dimensional photonic crystal (1DPC) constructed using multilayered porous TiO_2 takes advantage of the optical characteristics of the porous TiO_2 (PTO) layer. This renders it an exceptionally intriguing and versatile material for various applications. PTO possesses nanoscale dimensions and high surface area. They demonstrate remarkable chemical stability and corrosion resistance, making them biocompatible and non-toxic. One notable attribute of PTO has exceptional photocatalytic properties. They effectively harness light energy to facilitate chemical reactions, making them particularly valuable for applications in water treatment.[32,33] Additionally, porous TiO_2 photonic crystal (PTO-PC) can self-organize into ordered arrays, which proves advantageous for applications in photonics and optoelectronics. Furthermore, the synthesis of PTO nanotubes is relatively simple and cost-effective, making them easily accessible for research and potential large-scale applications.[34,35]

Tamm resonance has been successfully achieved in photonic crystals (PCs) for sensing techniques.[36–38] The structure involves depositing plasmonic metals such as Ag onto the PC. Tamm resonance occurs at the interface between the Ag and PC materials, resulting in localized optical resonance. This resonance improves the interaction between the sensing environment molecules and incident light, allowing for the detection of small variations or low concentrations.[39,40] Tamm sensor photonic crystals offer high sensitivity, a selective wavelength response, and an improved signal-to-noise ratio. They enable label-free detection, can be integrated with other optical components or systems, and reduce costs in the sensing process.

This work aims to explore the innovative application of Tamm sensor photonic crystals for detecting heavy metals, with a particular focus on mercury (Hg^{2+}) ions in water. The proposed structure involves a prism/Ag/cavity/porous TiO_2 photonic crystal (PTO-PC). The PTO-PC is composed of a ternary multilayer porous TiO_2 (PTO) layer. The optimization of layer thicknesses and porosity in the multilayer PTO is carried out to achieve superior sensor performance.

2. Design of sensor

The PTO-PC sensor design utilizes a ternary PC structure composed of three multilayers of PTO material, denoted as PTO_1, PTO_2, and PTO_3. These layers are repeated 10 times ($N = 10$) to enhance the interaction of light with the target sensing environment. The sensor is built on a prism with a refractive index of 1.4. A silver (Ag) layer is placed on a prism to enable plasmonic effects. Positioned above the Ag layer, a cavity layer acts as a confined reservoir, facilitating the introduction of polluted water containing Hg^{2+} heavy metal ions. The overall structure is represented as prism/Ag/cavity/$[PTO_1, PTO_2, PTO_3]^{N=10}$ as represented in Fig. 1.

The refractive indices of different materials are determined using specific equations and models. The complex refractive index for various concentrations of mercury ion solutions was obtained from the referenced paper.[41]

For the silver film, the Debye–Drude dispersion model is employed to characterize its relative permittivity (ε) using the equation[42,43]

$$\varepsilon = 1 - \frac{{\omega_p}^2}{\omega^2 + i\gamma\omega} \quad (1)$$

where $\omega_P = 136\,913 \times 10^{11}$ (rad s^{-1}) is the plasma frequency and $\gamma = 273.4494 \times 10^{11}$ (rad s^{-1}) is the damping frequency.[44] By taking the square root of ε, the refractive index (n) of silver can be obtained.

The refractive index of the TiO_2 layer varies with wavelength and is determined using the equation[45]

$$n_{TiO_2} = \sqrt{1 + \frac{4.6796\lambda^2}{\lambda^2 - (0.2002148)^2}} \quad (2)$$

where n_{TiO_2} represents the refractive index of TiO_2 and λ is the wavelength.

The Bruggeman effective medium approximation (BEMA) equation is used for calculating the effective refractive index (n_{eff}) of the PTO layer. This equation takes into account the refractive indices of TiO_2 (n_{TiO_2}) and the material filling the pores (n_v), as well as the porosity ratio (P). The equation is given by[46,47]

$$P\frac{{n_v}^2 - {n_{eff}}^2}{{n_v}^2 + 2{n_{eff}}^2} + (1-P)\frac{{n_{TiO_2}}^2 - {n_{eff}}^2}{{n_{TiO_2}}^2 + 2\,{n_{eff}}^2} = 0 \quad (3)$$

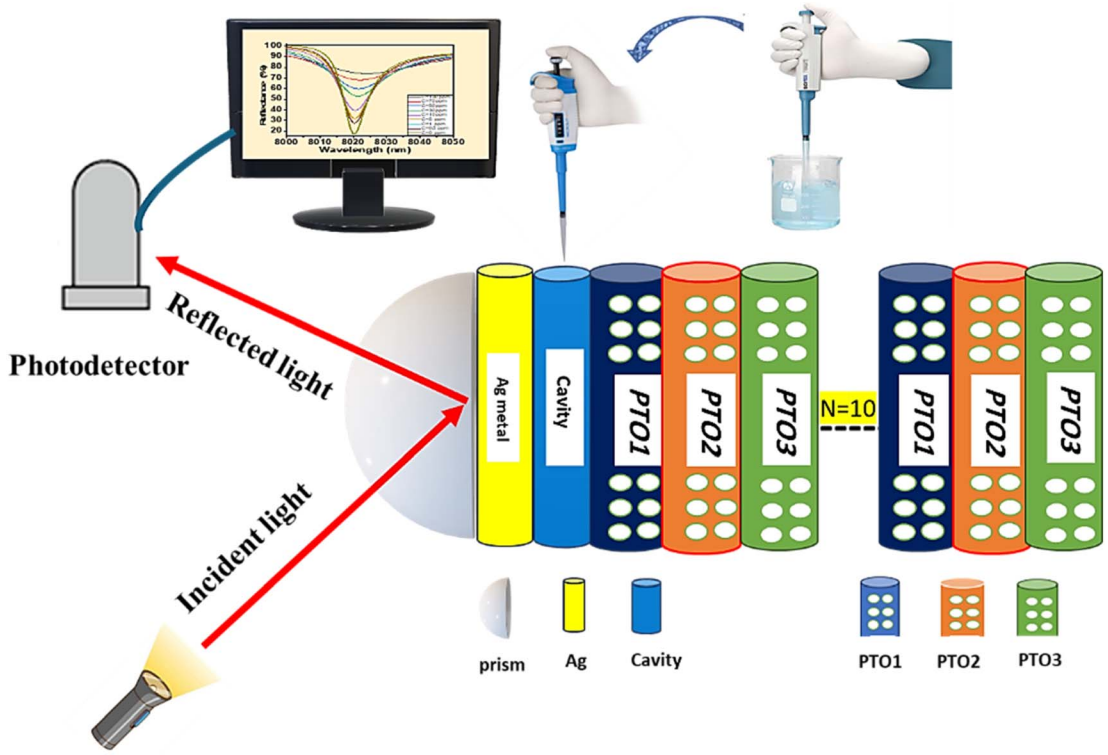

Fig. 1 Schematic diagram of the proposed sensor consisting of prism/Ag/cavity/PTO-PC.

Indeed, solving the BEMA equation provides valuable insights into the optical characteristics of the PTO layer.

Photonic crystals based on multilayer porous TiO_2 (PTO) layers can be fabricated using a conventional electrochemical anodizing method.[48] Typically, the anodization process is conducted in an electrochemical cell with two electrodes under ambient conditions. A Pt electrode is used as the counter electrode, while high-purity Ti foil serves as the working electrode in an HF aqueous electrolyte. Periodic variations in the applied voltage lead to changes in porosity and the effective refractive index, resulting in porous TiO_2 photonic crystals.[49] The Ag layer can be deposited onto the prism using a magnetron sputtering system.[50] The cavity is created by depositing a polymer such as benzocyclobutene (BCB) through spin coating on the Ag layer, followed by chemical etching.[51]

3. Theoretical model

The theoretical model employed in this study is built on the transfer matrix method (TMM).[52] This method allows us to analyze the reflectance characteristics of a periodic structure consisting of a prism/Ag/cavity/PTO-PC. The PC comprises multilayers, denoted as $[PTO_1/PTO_2/PTO_3]$.[10] By applying the TMM, the interaction between the incident light and the designed structure can be investigated. This interaction yields the overall optical characteristics of the structure, which can be derived using a subsequent matrix.[18]

The total transfer matrix for the proposed structure can be computed using eqn (4)

$$M = \begin{pmatrix} M_{11} & M_{12} \\ M_{21} & M_{22} \end{pmatrix} = (M_{Ag})(M_C)(M_{PTO_1}M_{PTO_2}M_{PTO_3})^N \quad (4)$$

Here, M_{11}, M_{12}, M_{21}, and M_{22} represent the elements of the total matrix. M_{Ag}, M_C, M_{PTO_1}, M_{PTO_2}, and M_{PTO_3} are the characteristic matrices of the Ag, cavity, PTO_1, PTO_2, and PTO_3 layers, respectively. The matrix of each layer in the structure is provided by

$$M_i = \begin{pmatrix} \cos\phi_i & \frac{-i}{\gamma_d}\sin\phi_i \\ -i\gamma_i \sin\phi_i & \cos\phi_i \end{pmatrix}, \quad (5)$$

$$\phi_i = \frac{2\Pi d_i}{\lambda} n_i \cos\theta_i, \quad \gamma_i = \sqrt{\frac{\varepsilon_0}{\mu_0}} n_1/\cos\theta_i \quad (6)$$

where i refers to the matrix for each layer in the structure, which can be Ag, cavity, PTO_1, PTO_2, and PTO_3. θ_i is the angle of incidence within layer i and d_i is the thickness of layer i. ε_0 and μ_0 are vacuum permittivity and permeability, respectively. The total characteristic matrix plays a vital role in calculating the reflectance coefficient of the structure.

$$r = \frac{M_{21}}{M_{11}} = \frac{(M_{11} + M_{12}\gamma_s)\gamma_0 - (M_{21} + M_{22}\gamma_s)}{(M_{11} + M_{12}\gamma_s)\gamma_0 + (M_{21} + M_{22}\gamma_s)} \quad (7)$$

where $\left(\gamma_{0,s} = \sqrt{\frac{\varepsilon_0}{\mu_0}} n_{0,s}/\cos\theta_{0,s}\right)$ for air (0) and prism substrate (s)

The $n_{0,s}$ represents the refractive index of both air (0) and prism substrate (s), while $\theta_{0,s}$ denotes the incident angle on the layer and

substrate, respectively. Lastly, the reflectance (R) is determined as the magnitude squared of the reflectance coefficient

$$R = |r^2| \tag{8}$$

4. Result and discussion

4.1 Reflectance spectra

Fig. 2 represents the reflectance spectra of electromagnetic (EM) waves. The spectra are plotted against the incident wavelength for two configurations: prism/PTO-PC and prism/cavity/PTO-PC. In both configurations, the pore of PTO is filled with pure water (0 ppm). The PC structure comprises three layers: PTO_1, PTO_2, and PTO_3. The thicknesses of these layers are specified as $d_1 = 850$ nm, $d_2 = 700$ nm, and $d_3 = 550$ nm, respectively. The corresponding porosities of the layers are $P_1 = 20\%$, $P_2 = 87\%$, and $P_3 = 15\%$. The layer sequence is repeated ten times within the structure.

In the prism/PTO-PC configuration, a photonic bandgap (PBG) is observed in the infrared (IR) spectrum, with a width of 2613.3 nm. The extensive width of the PBG is attributed to the significant difference in refractive indices between the layers of the structure. The PBG refers to a range of wavelengths in which the propagation of certain frequencies of light is forbidden within the structure. It arises as a result of the interference and scattering of light waves within the periodic layers of the photonic crystal. Additionally, the presence of ripples outside PBG can be attributed to the constructive and destructive interference effects within the PC structure. When a 12 μm-thick cavity layer is introduced in front of the existing PTO multilayer, the resulting configuration is known as prism/cavity/PTO-PC. The presence of the cavity layer does not affect the reflectance and does not provide an opportunity for resonance to occur. The primary function of the cavity layer is to accommodate the analyte within the structure.

4.1.2 Sensing prism/Ag/cavity/PTO-PC structure. In the prism/Ag/cavity/PTO-PC configuration, a 10 nm-thick Ag layer to the upper part of the structure significantly enhances the photonic bandgap (PBG). This enhancement results in a broad PBG that spans a wide range of wavelengths, as depicted in Fig. 3. Furthermore, the spectrum exhibits the presence of the Tamm resonance mode, which arises from the trapping of light waves between the silver layer and the PTO-PC.[53] Specifically, at a heavy metal concentration of 0 ppm (pure water), the Tamm resonance mode is detected at a wavelength of 8020.2 nm. The presence of a heavy metal solution in the cavity layer impacts the Tamm resonance conditions. When the cavity is filled with a 100 ppm Hg^{2+} ions solution, the Tamm mode shifts to a new position at 8024.7 nm. The Tamm mode greatly improves the effectiveness and performance of the suggested sensor.

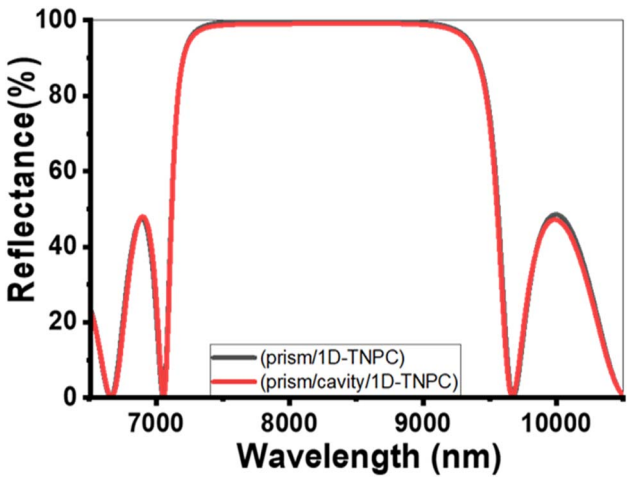

Fig. 2 Reflectance spectra at 0 ppm (pores filled with pure water) for the (a) prism/PTO-PC and (b) prism/cavity/PTO-PC.

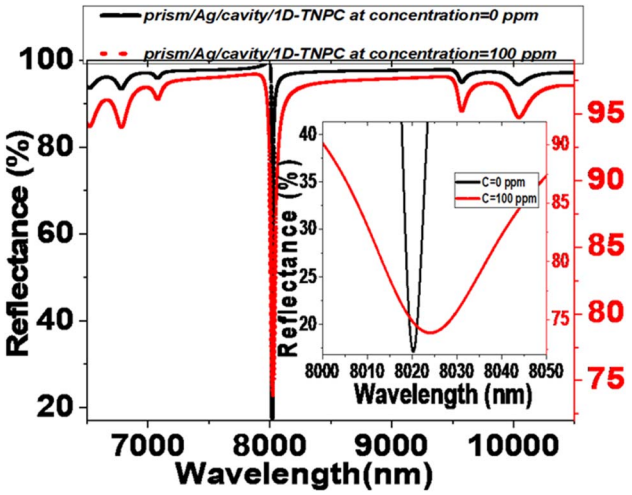

Fig. 3 Reflectance spectra of the prism/Ag/cavity/PTO-PC at (a) 0 ppm (pure water) and (b) 100 ppm.

The red shift observed in the reflectance spectra in the presence of Hg^{2+} ions is due to changes in the optical properties of the sensor's structure. As the concentration of Hg^{2+} ions increase, the refractive index of the sensing medium also increases. Hg^{2+} ions diffuse into the porous TiO_2 layers and the cavity, raising the refractive indices of these components. This increase in refractive index alters the phase shift of the standing wave conditions within the sensor.[54] As a result, the resonant defect mode shifts to longer wavelengths in accordance with the Bragg–Snell law.[55,56]

The sensor's sensitivity (S) has been determined by evaluating the relationship between the change in position of the Tamm resonance mode ($\Delta\lambda_T$) and the corresponding variations in heavy metal concentrations (ΔC). It is calculated using the equation[18]

$$S = \Delta\lambda_T / \Delta C = \frac{\lambda_{100} - \lambda_0}{C_{100} - C_0} = \frac{\lambda_{100} - \lambda_0}{100 - 0} \tag{9}$$

where, λ_{100} and λ_0 are the Tamm resonance positions corresponding to Hg^{2+} ions concentrations of $C_{100} = 100$ ppm and $C_0 = 0$ ppm, respectively.

From the data in Fig. 3, $S = \frac{\Delta\lambda_T}{\Delta C} = \frac{\lambda_{100} - \lambda_0}{C_{100} - C_0} = \frac{8024.3 - 8020.4}{100} = 0.039$ nm ppm^{-1}.

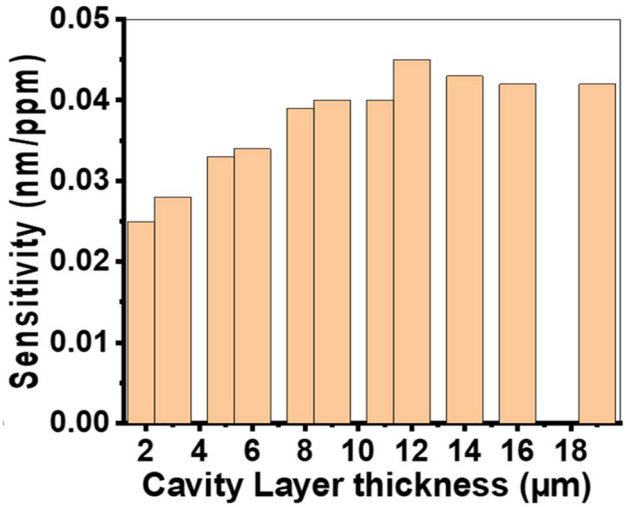

Fig. 4 The sensitivity of the suggested sensor varies with the thickness of the cavity layer at $N = 10$, $P_1 = 20\%$, $P_2 = 87\%$, $P_3 = 15\%$, $d_{Ag} = 10$ nm, $d_1 = 850$ nm, $d_2 = 700$ nm, and $d_3 = 550$ nm.

4.2 Optimization of parameters

The proposed structure undergoes parameter adjustments to improve the sensitivity and overall performance of the sensor design. The optimization focuses on optimizing the porosities and thicknesses of all layers in the following sections. During the optimization process, the reflectivity is calculated as a function of the incidence wavelength to determine the Tamm mode position at two different concentrations (0 and 100 ppm) using eqn (8). Then, the shift in Tamm mode position corresponds is variations in heavy metal concentrations used to determine the sensitivity using eqn (9).

4.2.1 Cavity layer thickness. The sensitivity of the prism/Ag/cavity/PTO-PC configuration is influenced by the thickness of the cavity layer (d_c). Fig. 4 illustrates the calculated sensitivity as a function of the cavity layer thickness, ranging from 2000 to 19 000 nm. The structure parameters used are $N = 10$, $P_1 = 20\%$, $P_2 = 87\%$, $P_3 = 15\%$, $d_{Ag} = 10$ nm, $d_1 = 850$ nm, $d_2 = 700$ nm, and $d_3 = 550$ nm.

The sensitivity value gradually increases and then decreases, as shown in Fig. 4. The maximum sensitivity of 0.045 nm RIU^{-1} is achieved when the cavity layer thickness is 12 000 nm. Changes in the thickness of the cavity layer modify the path of the incident light, influencing optical interferences within the prism/Ag/cavity/PTO-PC structure. A very thin cavity layer fails to support constructive interference, resulting in weak plasmon resonance. Conversely, an excessively thick cavity layer dissipates the energy of the plasmon wave, reducing coupling. Therefore, the optimal cavity layer thickness for maximizing sensor sensitivity is determined to be 12 000 nm.

4.2.2 Thicknesses of PTO layers. This section focuses on investigating the impact of varying the thickness of PTO layers, specifically d_1, d_2, and d_3, on the sensitivity of the sensor. The other parameters remain constant as previously mentioned ($N = 10$, $P_1 = 20\%$, $P_2 = 87\%$, $P_3 = 15\%$, $d_{Ag} = 10$ nm, and $d_c = 12$ 000 nm). The obtained results demonstrate that sensitivity

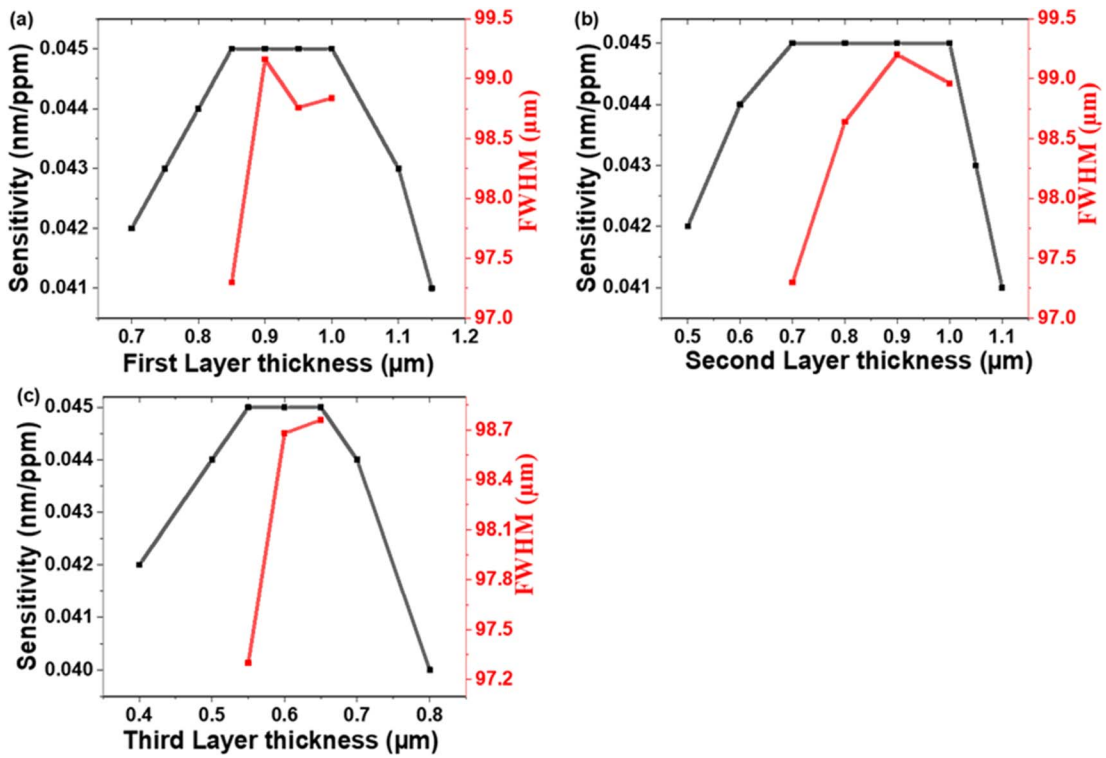

Fig. 5 The sensitivity and FWHM of the suggested sensor as a function of the thicknesses (a) 1st layer thickness, (b) 2nd layer thickness and (c) 3rd layer thickness of the PTO layers at $N = 10$, $d_{Ag} = 10$ nm, $d_c = 12\,000$ nm, $P_1 = 20\%$, $P_2 = 87\%$, and $P_3 = 15\%$.

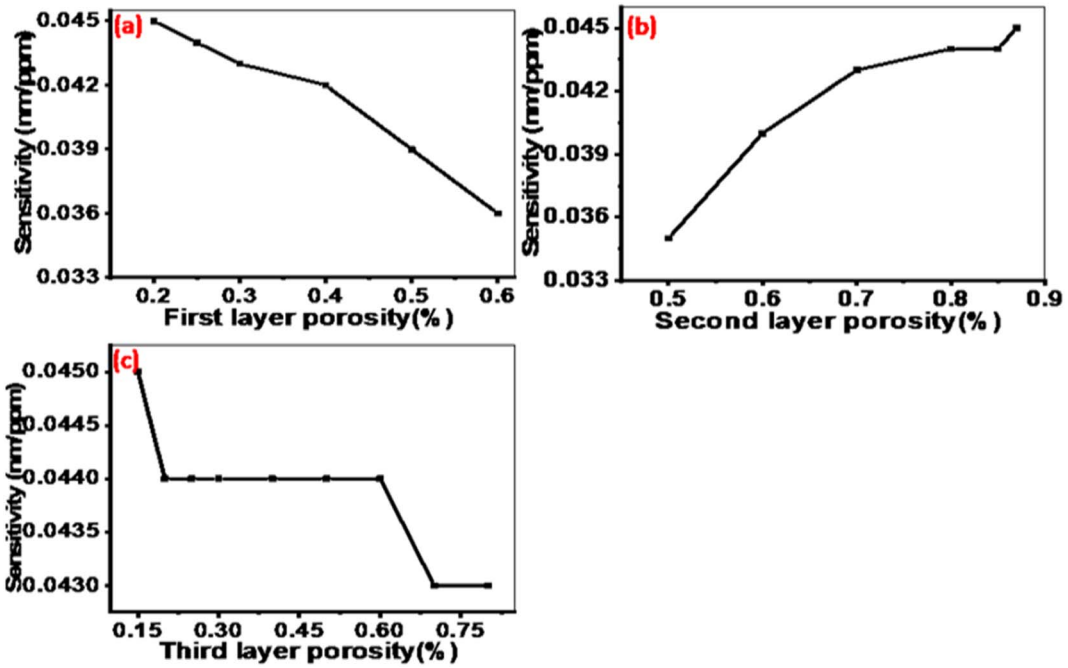

Fig. 6 The sensitivity of the designed sensor as a function of the porosities for layers (a) P_1, (b) P_2, and (c) P_3 at $N = 10$, $d_1 = 850$ nm, $d_2 = 700$ nm, $d_3 = 550$ nm, $d_{Ag} = 10$ nm, and $d_c = 12\,000$ nm.

increases as the thickness of the PTO layers is increased. It reaches a plateau and remains constant within a certain range of thickness values before gradually declining. This trend is visually depicted in Fig. 5. The incident light is a partial transmission and reflection of light at each interface between the PTO layers. This results in constructive or destructive interference within the structure. The presence of a cavity in the PC leads to the confinement of electromagnetic waves at the resonance frequency of the defect mode. The formation of this defect mode is influenced by light interference within the PC. Optimizing the thickness of the PTO layers is required to enhance light confinement in the cavity. If the cavity layer is either too thin or too thick, the localization of light becomes weak, leading to reduced sensitivity.[57]

To evaluate the sensor's performance, the full width at half-maximum (FWHM) of the resonance mode is a crucial factor.[58] A narrower FWHM corresponds to a sharper and more precise resonance, indicating higher resolution and better sensor performance. Therefore, minimizing the FWHM is essential for optimizing the sensor's sensitivity and accuracy.[59] Fig. 5(a)–(c) presents the behavior of FWHM concerning the thicknesses of the PTO layers. Based on the observed low FWHM values, the optimal thicknesses for the PTO layers are determined as follows: $d_1 = 850$ nm, $d_2 = 700$ nm, and $d_3 = 550$ nm. These specific thickness values are selected to achieve a narrow resonant dip and enhance the sensor's resolution.

4.2.3 Effect of porosities of layers P_1, P_2, and P_3. To achieve the highest sensitivity for detecting Hg^{2+} metal ions in water, the effect of varying the porosity of layers P_1, P_2, and P_3 in the proposed PC structure was investigated. The following parameters were kept constant: $N = 10$, $d_1 = 850$ nm, $d_2 = 700$ nm, $d_3 = 550$ nm, $d_{Ag} = 10$ nm, and $d_c = 12\,000$ nm.

Fig. 6(a) illustrates the sensitivity behavior when the porosity of the first layer is changed from 20% to 60%. It can be observed that sensitivity gradually decreases with increasing porosity, indicating that the optimal porosity value for the first layer is 20%. Similarly, Fig. 6(b) depicts the sensitivity trend as the porosity of the second layer varied from 50% to 87%. It shows that sensitivity increases gradually with increasing porosity, suggesting that the optimal porosity value for the second layer is 87%. In Fig. 6(c), the porosity of the third layer is varied from 15% to 80%. The highest sensitivity is obtained at a porosity of 15% and then decreases beyond that point.

The obtained results demonstrate that the sensitivity of the proposed sensor structure is influenced by the porosities of the PTO layers. The refractive index of the PTO layer is directly related to its porosity as described by eqn (3). This relationship allows for the estimation of changes in the average refractive behavior of the composite material as the proportion of voids within it varies.[60] Specifically, as the porosity of the PTO layers increases, their effective refractive index decreases. This occurs because higher porosity introduces more voids, which reduces the overall density of the TiO_2 material and thus lowers its refractive index. Optimizing the porosities of the PTO layers is crucial because it affects the phase shift of light interference within the sensor, as outlined in eqn (3) and (6). The phase shift influences the reflection spectrum of the sensor, which, in turn, affects its sensitivity. The optimal values for the porosities of the layers were determined to be $P_1 = 20\%$, $P_2 = 87\%$, and $P_3 = 15\%$ as shown in Fig. 6.

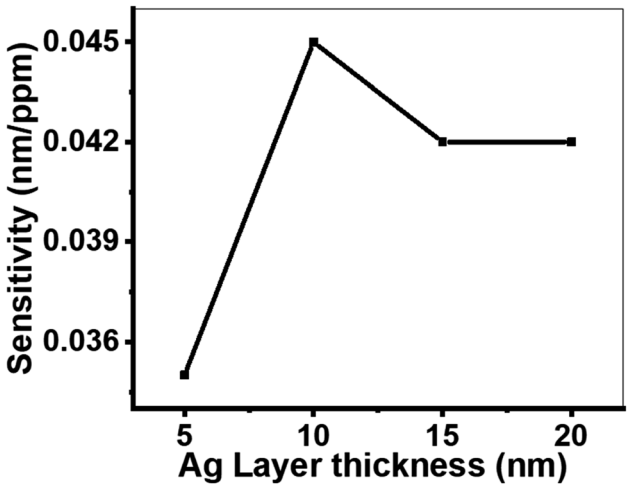

Fig. 7 The sensitivity of the designed sensor as a function of the silver layer thickness at $N = 10$, $d_1 = 850$ nm, $d_2 = 700$ nm, $d_3 = 550$ nm, $P_1 = 20\%$, $P_2 = 87\%$, $P_3 = 15\%$, and $d_c = 12\,000$ nm.

4.2.4 Effect of thickness of Ag layer. The thickness of the Ag layer plays a crucial role in the propagation of surface plasmons and the coupling of light to these plasmons, which directly impacts the sensitivity of the SPR sensor. To optimize sensitivity for detecting Hg^{2+} in water, the effect of varying the Ag thickness was investigated as shown in Fig. 7. The following parameters were kept constant: $N = 10$, $P_1 = 20\%$, $P_2 = 87\%$, $P_3 = 15\%$, $d_c = 12\,000$ nm, $d_1 = 850$ nm, $d_2 = 700$ nm, and $d_3 = 550$ nm. The highest sensitivity was observed at an Ag layer thickness of 10 nm. In contrast, thicknesses of 5, 15, and 20 nm resulted in lower sensitivity due to poor resonance and suboptimal sensor performance. A 10 nm Ag layer thickness allows for efficient coupling of light to the surface plasmons, yielding high sensitivity. When the Ag layer is too thin (*e.g.*, 5 nm), the surface plasmons are poorly confined, leading to reduced sensitivity. Conversely, a thicker Ag layer (*e.g.*, 15 or 20 nm) prevents effective light penetration, also resulting in low sensitivity.[61,62]

4.2.5 Performance analysis of optimized sensor. Based upon the studies conducted in the preceding sections, the optimized parameters for the sensor are as follows: $N = 10$, $P_1 = 20\%$, $P_2 = 87\%$, $P_3 = 15\%$, $d_{Ag} = 10$ nm, $d_c = 12\,000$ nm, $d_1 = 850$ nm, $d_2 = 700$ nm, and $d_3 = 550$ nm. The sensor is designed to operate at room temperature, and small temperature changes do not significantly impact its sensitivity. This is due to the stability of the materials used in the sensor across a range of temperatures.

Fig. 8(a) illustrates the change in the resonance mode shape and reflectance values as the concentration of Hg^{2+} metal ions increases from 0 ppm to 5, 10, 30, 50, 70, and 100 ppm, under the ideal conditions. The reflection peak flattens considerably with increasing Hg^{2+} ions concentration, indicating reduced diffraction. Fig. 8(b) demonstrates the resonance intensity as a function of Hg^{2+} ions concentration. The Tamm resonance intensity increases with the concentration, reaching a minimum value of 17.17 at 0 ppm and a maximum value of 74.34 at 100 ppm. Hence, the suggested sensor exhibits a strong response to varying concentrations of Hg^{2+} metal ions,

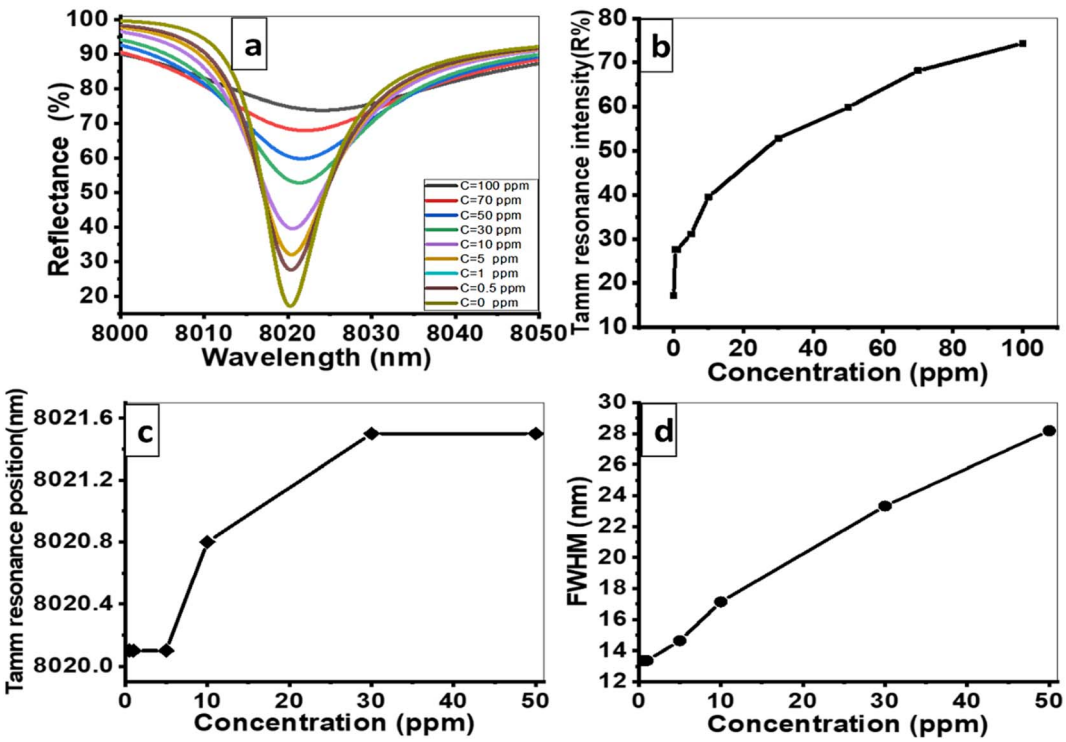

Fig. 8 The reflectance of the optimum structure as a function of wavelength at different concentrations of Hg^{2+} ions solution (b–d) represents the intensity, position of the resonant peak, and FWHM as functions of the concentration of Hg^{2+} ions solution, respectively.

Table 1 Properties of the proposed sensor based on photonic crystals for various Hg^{2+} ions concentrations in water (ppm)

Hg^{2+} ions concentration (ppm)	FoM (ppm^{-1})	QF
0	—	600.3
5	—	548.2
10	4.08×10^{-3}	467.96
30	2.00×10^{-3}	343.98
50	9.94×10^{-4}	284.7
70	8.22×10^{-4}	219.8
100	9.19×10^{-4}	175.6

highlighting its sensitivity. In Fig. 8(c), the spectral position of the Tamm dips shifts to higher wavelengths with increasing concentrations of Hg^{2+} metal ions. This shift is attributed to the alteration of the guided mode resonance as the Hg^{2+} ions concentration rises. These changes in the resonance peak position further emphasize the sensor's sensitivity to even small variations in the concentration of Hg^{2+} metal ions. Fig. 8(d) describes the relationship between the FWHM and the Hg^{2+} ions concentration. The FWHM tends to increase with the Hg^{2+} ions concentration due to the imaginary parts of the refractive index for Hg^{2+} ions.

Many parameters including sensitivity, quality factor (QF), and figure of merit (FoM) used to evaluate the performance of the proposed sensor.[18] These parameters can be calculated using eqn (10) and (11). The values are presented in Table 1. From 0 to 100 ppm, the FoM increases from 4.08×10^{-3} to 9.19×10^{-4}, while the QF decreases from 600.3 to 175.6.

$$\mathrm{QF} = \lambda_T/\mathrm{FWHM} \quad (10)$$

$$\mathrm{FoM} = S/\mathrm{FWHM} \quad (11)$$

5. Conclusions

This study introduced a novel structure for sensing Hg^{2+} ions concentration utilizing a ternary one-dimensional photonic crystal. The sensor relies on the generation of Tamm resonance within a photonic crystal composed of Ag and porous TiO_2 layers. The sensitivity of the sensor was determined to be 0.045 nm ppm^{-1}. These promising results have inspired future research endeavors, focusing on the development of tailored photonic crystals as nanophotonic devices for heavy metal sensing applications.

Data availability

The data that support the findings of this study are available from the corresponding author upon reasonable request.

Conflicts of interest

There are no conflicts to declare.

References

1 K. H. Vardhan, P. S. Kumar and R. C. Panda, *J. Mol. Liq.*, 2019, **290**, 111197.
2 C. F. Carolin, P. S. Kumar, A. Saravanan, G. J. Joshiba and M. Naushad, *J. Environ. Chem. Eng.*, 2017, **5**, 2782–2799.
3 C. FN, M. MF and J. Ecosyst, *Ecography*, 2017, **7**, 5–8.
4 A. H. M. Almawgani, J. Surve, T. Parmar, A. Armghan, K. Aliqab, G. A. Ali and S. K. Patel, *Photonics*, 2023, **10**, 56.
5 L. Burratti, E. Sgreccia, F. Bertelà and F. Galiano, *Chemosphere*, 2024, **362**, 142636.
6 Z. A. Alrowaili, H. Makhlouf Fathy, H. A. Elsayed, M. Aouassa, M. H. Mahmoud, K. S. El-Nasser, T. A. Taha and A. Mehaney, *Ultrasonics*, 2023, **130**, 106928.
7 A. Kumar, M. Cabral-Pinto, A. Kumar, M. Kumar and P. A. Dinis, *Appl. Sci.*, 2020, **10**, 7078.
8 M. M. S. Cabral Pinto, M. M. V. Silva, E. A. Ferreira da Silva and A. P. Marinho-Reis, *Geosci.*, 2017, **7**, 78.
9 Y. Pu, Z. Gu, T. F. H. Bovee, Y. Yang, Y. Ying, M. Li and X. Hong, *Food Chem.*, 2024, 140354.
10 K. H. Kim, E. Kabir and S. A. Jahan, *J. Hazard. Mater.*, 2016, **306**, 376–385.
11 A. M. Elsayed, A. M. Ahmed, M. T. Tammam, M. F. Eissa and A. H. Aly, *Sci. Rep.*, 2024, **141**, 1–9.
12 L. A. Malik, A. Bashir, A. Qureashi and A. H. Pandith, *Environ. Chem. Lett.*, 2019, **17**, 1495–1521.
13 B. K. Bansod, T. Kumar, R. Thakur, S. Rana and I. Singh, *Biosens. Bioelectron.*, 2017, **94**, 443–455.
14 Y. Wang, X. Wang, J. Mu, H. Yu, X. Lv, T. Liang and C. Cheng, *Chem. Eng. Sci.*, 2024, **299**, 120473.
15 F. A. Sayed, H. A. Elsayed, M. Al-Dossari, M. F. Eissa, A. Mehaney and A. H. Aly, *Sci. Rep.*, 2023, **13**, 21793.
16 P. Kurup, C. Sullivan, R. Hannagan, S. Yu, H. Azimi, S. Robertson, D. Ryan, R. Nagarajan, T. Ponrathnam and G. Howe, *Indian Geotech. J.*, 2017, **47**, 421–436.
17 Q. Chen, Y. Yao, X. Li, J. Lu, J. Zhou and Z. Huang, *J. Water Process Eng.*, 2018, **26**, 289–300.
18 A. M. Elsayed, A. M. Ahmed and A. H. Aly, *Appl. Opt.*, 2022, **61**, 1668.
19 Z. A. Alrowaili, M. Aouassa, M. H. Mahmoud, K. S. El-Nasser, H. A. Elsayed, T. A. Taha, A. M. Ahmed, A. Hajjiah and A. Mehaney, *J. Mol. Liq.*, 2023, **369**, 120964.
20 A. H. Aly and H. A. Elsayed, *Phys. Scr.*, 2019, **94**, 125501.
21 H. A. Elsayed and A. Mehaney, *Appl. Nanosci.*, 2021, **11**, 149–157.
22 A. M. Ahmed, H. A. Elsayed and A. Mehaney, *Plasmonics*, 2021, **16**, 547–557.
23 M. Shaban, A. M. Ahmed, E. Abdel-Rahman and H. Hamdy, *Sci. Rep.*, 2017, **71**(7), 1–10.
24 D. Devashish, O. S. Ojambati, S. B. Hasan, J. J. W. Van Der Vegt and W. L. Vos, *Phys. Rev. B*, 2019, **99**, 075112.
25 F. Segovia-Chaves, H. A. Elsayed, A. Mehaney and A. M. Ahmed, *Optik*, 2021, **242**, 167161.
26 N. R. Ramanujam, H. J. El-Khozondar, V. Dhasarathan, S. A. Taya and A. H. Aly, *Phys. B Condens. Matter*, 2019, **572**, 42–55.

27 T. Li, G. Liu, H. Kong, G. Yang, G. Wei and X. Zhou, *Coord. Chem. Rev.*, 2023, **475**, 214909.
28 L. Lu, X. Dong, Z. Liu, J. Wei, J. Li, H. Zhou, J. Zhu and X. Shi, *Dyes Pigm.*, 2021, **195**, 109676.
29 T. A. Taha, A. Mehaney and H. A. Elsayed, *Mater. Chem. Phys.*, 2022, **285**, 126125.
30 P. C. Chou, S. H. Chen, C. J. Chang, C. H. Lu and J. K. Chen, *Appl. Surf. Sci.*, 2022, **585**, 152718.
31 A. Das, P. K. Panigrahi, G. Palai and R. Satpathy, *J. Opt.*, 2024, **1–9**, DOI: **10.1007/s12596-024-01744-x**.
32 A. M. Elsayed, M. Shaban, A. H. Aly, A. M. Ahmed and M. Rabia, *Mater. Sci. Semicond. Process.*, 2022, **139**, 106348.
33 A. M. Elsayed, M. Rabia, M. Shaban, A. H. Aly and A. M. Ahmed, *Sci. Rep.*, 2021, **111**, 1–12.
34 J. Huang, H. Ren, X. Liu, X. Li and J. J. Shim, *Superlattices Microstruct.*, 2015, **81**, 16–25.
35 W. T. Kim and W. Y. Choi, *Sens. Actuators, A*, 2017, **260**, 178–184.
36 Z. A. Zaky, M. R. Singh and A. H. Aly, *Photonics Nanostructures: Fundam. Appl.*, 2022, **49**, 100995.
37 Z. Wang, C. Wang, F. Sun, Z. Fu, Z. Xiao, J. Wang and H. Tian, *J. Opt. Soc. Am. B*, 2019, **36**, 215.
38 A. Juneau-Fecteau and L. G. Fréchette, *Opt. Mater. Express*, 2018, **8**, 2774.
39 B. Auguié, M. C. Fuertes, P. C. Angelomé, N. L. Abdala, G. J. A. A. Soler Illia and A. Fainstein, *ACS Photonics*, 2014, **1**, 775–780.
40 A. M. Ahmed and A. Mehaney, *Sci. Rep.*, 2019, **9**, 1–9.
41 Y. W. Fen and W. M. M. Yunus, *Opt. Photonics J.*, 2011, **01**, 116–123.
42 H. Gai, J. Wang and Q. Tian, *Appl. Opt.*, 2007, **46**, 2229–2233.
43 C. J. Wu, Y. H. Chung, B. J. Syu and T. J. Yang, *Prog. Electromagn. Res.*, 2010, **102**, 81–93.
44 M. R. Querry, M. A. Ordal, R. J. Bell, L. L. Long and R. W. Alexander, *Appl. Opt.*, 1985, **24**(24), 4493–4499.
45 *Refractive Index of TiO_2 (Titanium Dioxide) – Bodurov*, **https://refractiveindex.info/?shelf=main&book=TiO2&page=Bodurov**, accessed 28 August 2021.
46 D. G. Mohan, S. Gopi, V. Rajasekar, K. Krishnan, D. G. Mohan, S. Gopi, L. Selvarajan, R. Rajavel, B. Prakash, D. G. Mohan, S. Gopi, A. A. Alloys, U. Taguchi, L. Selvarajan, R. Sasikumar, D. G. Mohan, P. Naveen Kumar and V. Muralidharan, *Mater. Today Proc.*, 2019, **27**, 31.
47 S. Farsinezhad, A. Mohammadpour, A. N. Dalrymple, J. Geisinger, P. Kar, M. J. Brett and K. Shankar, *J. Nanosci. Nanotechnol.*, 2013, **13**, 2885–2891.
48 Y. Fu and A. A. Mo, *Nanoscale Res. Lett.*, 2018, **13**, 187.
49 O. Zakir, R. Idouhli, M. Elyaagoubi, M. Khadiri, A. Aityoub, Y. Koumya, S. Rafqah, A. Abouelfida and A. Outzourhit, *J. Nanomater.*, 2020, **2020**, 4745726.
50 E. T. Hu, H. Zhao, M. Wang, J. Wang, Q. Y. Cai, K. Yu and W. Wei, *Nanomater*, 2023, **13**, 2108.
51 S. Chowdhury, *Microelectron. Reliab.*, 2022, **138**, 114689.
52 A. H. M. Almawgani, H. M. Fathy, G. A. Ali, H. A. Elsayed and A. Mehaney, *Micromachines*, 2023, **14**, 204.
53 S. Kumar, M. K. Shukla, P. S. Maji and R. Das, *J. Phys. D Appl. Phys.*, 2017, **50**, 375106.
54 A. H. Aly, Z. A. Zaky, A. S. Shalaby, A. M. Ahmed and D. Vigneswaran, *Phys. Scr.*, 2020, **95**, 035510.
55 A. M. Ahmed, M. Shaban and A. H. Aly, *Optik*, 2017, **145**, 121–129.
56 N. Ayyanar, P. G. Kuppusamy, G. Thavasi Raja, D. Vigneswaran and A. H. Aly, *IET Optoelectron.*, 2019, **13**(3), 118–123.
57 J. Tang, Y. Ye, J. Xu, Z. Zheng, X. Jin, L. Jiang, J. Jiang and Y. Xiang, *Nanomaterials*, 2020, **10**(3), 500.
58 Q. Q. Meng, X. Zhao, C. Y. Lin, S. J. Chen, Y. C. Ding and Z. Y. Chen, *Sensors*, 2017, **17**, 1846.
59 Z. A. Zaky, A. M. Ahmed, A. S. Shalaby and A. H. Aly, *Sci. Rep.*, 2020, **10**, 9736.
60 T. Galy, M. Marszewski, S. King, Y. Yan, S. H. Tolbert and L. Pilon, *Microporous Mesoporous Mater.*, 2020, **291**, 109677.
61 M. Mohamedi, F. Challali, T. Touam, M. Konstantakopoulou, V. Bockelée, D. Mendil, S. Ouhenia, D. Djouadi and A. Chelouche, *Appl. Phys. A: Mater. Sci. Process.*, 2023, **129**, 1–16.
62 O. Pluchery, R. Vayron and K. M. Van, *Eur. J. Phys.*, 2011, **32**, 585.